


## Reversible-to-irreversible transition of colloidal polycrystals under cyclic athermal quasistatic deformation

Khushika,<sup>1</sup> Lasse Laurson,<sup>2</sup> and Pritam Kumar Jana <sup>1,\*</sup>

<sup>1</sup>*Department of Chemistry, Birla Institute of Technology and Science, Pilani, Pilani Campus, Rajasthan 333031, India*

<sup>2</sup>*Computational Physics Laboratory, Tampere University, P.O. Box 692, FI-33014 Tampere, Finland*



(Received 8 August 2023; accepted 29 November 2023; published 21 December 2023)

Cyclic loading on granular packings and amorphous media exhibits a transition from reversible elastic behavior to irreversible plasticity. The present study compares the irreversibility transition and microscopic details of colloidal polycrystals under oscillatory tensile-compressive and shear strain. Under both modes, the systems exhibit a reversible to irreversible transition. However, the strain amplitude at which the transition is observed is larger in the shear strain than in the tensile-compressive mode. The threshold strain amplitude is confirmed by analyzing the dynamical properties, such as mobility and atomic strain (von Mises shear strain and the volumetric strain). The structural changes are quantified using a hexatic order parameter. Under both modes of deformation, dislocations and grain boundaries in polycrystals disappear, and monocrystals are formed. We also recognize the dislocation motion through grains. The key difference is that strain accumulates diagonally in oscillatory tensile-compressive deformation, whereas in shear deformation, strain accumulation is along the  $x$  or  $y$  axis.

DOI: [10.1103/PhysRevE.108.064612](https://doi.org/10.1103/PhysRevE.108.064612)

### I. INTRODUCTION

A large number of periodically driven soft materials, including disordered granular media [1–3], colloidal suspensions [4–7], and colloidal gels [8], exhibit an intriguing transition from reversible, elastic behavior to irreversible, plastic deformation as the applied strain amplitude overcomes a threshold value [9–15]. It is important to understand the origin of irreversibility from reversible microscopic dynamics because it may shed light on the nature of yielding in those systems. For example, in a crystalline system, yielding is mediated by defects motion. For amorphous solids, localized rearrangements, known as shear transformations, are considered to be responsible for flow [17]. However, the identification of those local events due to their disordered structure is challenging. In recent work, the connection between irreversibility transition with yielding of amorphous solids and jamming was established by investigating the response of soft-sphere assemblies to athermal cyclic-shear deformation over a variety of densities and amplitudes of deformation [16,17]. The relation between yielding in crystals and glasses is still a subject of current investigation [18].

In between those two classes of materials, crystals and amorphous solids, lie polycrystals, in which several crystalline regions are separated by grain boundaries. The grain boundaries in polycrystalline materials can control bulk properties such as electrical conductivity, yield strength, etc. For example, the yield strength of the materials can be improved by increasing the density of grain boundaries [19]. This structure-property relationship is even more interesting in

two-dimensional (2D) materials in which grain boundaries can translate, create new boundaries, or be annihilated entirely from the system under external forces [20].

Colloidal particles are considered scaled-up models of atoms. Colloidal suspensions are systems widely used to directly observe phenomena that would otherwise not be within experimental reach. They can be assembled into colloidal polycrystals, in which ordered crystalline regions are separated by extended grain boundaries formed by dislocation arrays [21–24]. The application of a cyclic deformation to colloidal polycrystals allows us to follow at the same time dynamics of individual particles (“atoms”) and the large-scale response of the polycrystalline texture [21–24]. Plastic deformation of colloidal polycrystals has been studied in experiments and simulations [24–26]. In a previous study in which we applied oscillatory shear deformation to polycrystalline samples, a nonequilibrium phase transition mediated by the motion of defects and controlled by the strain amplitude was observed [27]. Experiments of plastic flow have also been performed under uniaxial stress in metallurgy, amorphous metals [28], and granular materials [29]. A detailed comparison of the motion of defects that leads to nonequilibrium phase transition in different modes of deformations may shed light on the microscopic dynamics associated with the process.

In the present study, we explore the irreversibility transition in 2D polycrystalline samples under oscillatory tension-compression and shear deformation by employing the athermal quasistatic method. The results reveal that under both deformation modes, the system exhibits a reversible to irreversible transition. The threshold strain amplitude after which irreversibility is observed is larger in the case of the oscillatory shear deformation. We confirmed this by analyzing

\*pritam.jana@pilani.bits-pilani.ac.in

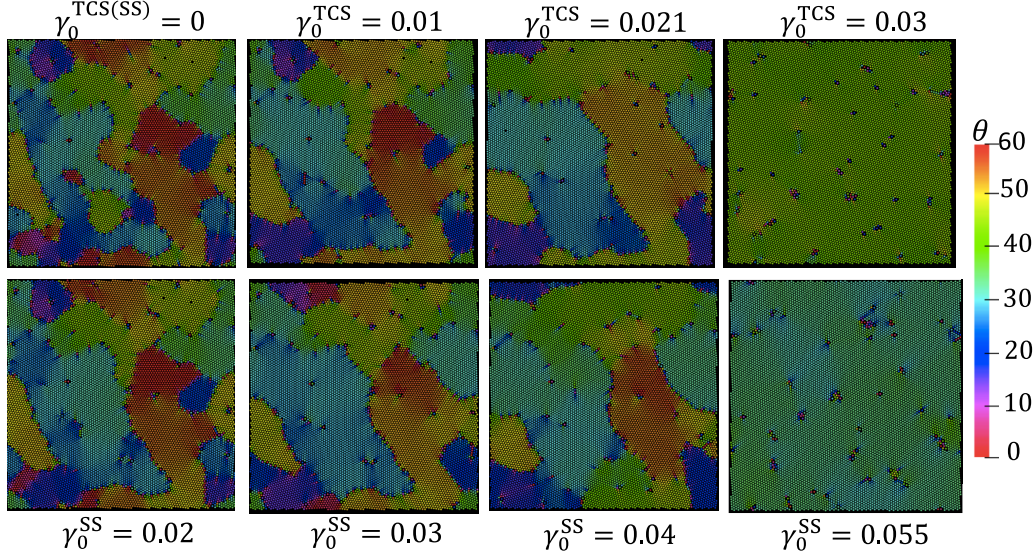


FIG. 1. Local grain orientations are shown after the completion of 200 cycles for different strain amplitudes.  $\gamma_0^{\text{TCS(SS)}} = 0$  denotes the initial configuration of the sample, i.e., without any deformation. The top row is for tensile-compressive strain, and the bottom row is for shear strain.

dynamical properties, such as mobility and atomic strain, and structural behavior, such as hexatic order parameters. Under both modes of deformation, we observe the disappearance of dislocations and grain boundaries and the formation of monocrystals with some defects because of the particles with larger sizes. The mechanism of monocrystal formation is also identified, and a key difference is that in the case of oscillatory tensile-compressive loading, the strain accumulates diagonally, whereas in oscillatory shear strain, the strain accumulation is along the  $x$  or  $y$  axis. This paper is organized as follows: In Sec. II we describe the model and simulation details, and the analysis, results, and discussion are presented in Sec. III. Finally, the concluding remarks are made in Sec. IV.

## II. MODEL AND SIMULATION DETAILS

We consider a two-dimensional system with two types of particles, large ( $l$ ) and small ( $s$ ). They interact via a pairwise Lennard-Jones potential,

$$V_{\alpha\beta}(r) = 4\epsilon_{\alpha\beta} \left[ \left( \frac{\sigma_{\alpha\beta}}{r} \right)^{12} - \left( \frac{\sigma_{\alpha\beta}}{r} \right)^6 \right] - V_{\alpha\beta}(r_c), \quad (1)$$

where  $r$  is the distance between a particle of type  $\alpha$  and one of type  $\beta$  ( $\alpha, \beta = l, s$ ). The function  $V_{\alpha\beta}(r) = 0$  when  $r > r_c^{\alpha\beta}$ , a cutoff distance, and  $V_{\alpha\beta}(r_c)$  ensures that  $V_{\alpha\beta}(r)$  is continuous at  $r = r_c^{\alpha\beta}$ . The parameters of the potential are chosen as follows:  $\sigma \equiv \sigma_s = 1.0$ ,  $\sigma_l = 1.4\sigma$ , and  $\sigma_{ls} = 1.2\sigma$ , where  $\sigma_{\alpha,\beta}$  is the finite distance at which the interparticle ( $\alpha, \beta$ ) potential becomes zero (the particle diameter), and  $\epsilon \equiv \epsilon_{ll} = 1.0$ ,  $\epsilon_{ss} = 0.5\epsilon$ , and  $\epsilon_{ls} = 1.5\epsilon$  are the energy parameters. The cutoff distance  $r_c^{\alpha\beta}$  is fixed to  $3.0\sigma_{\alpha\beta}$ . The typical numbers of particles used in the system are  $N_l = 50$  and  $N_s = 10\,000$ , with  $m = 1$  for both. The typical length of a 2D simulation box is  $L = 100\sigma$ . The unit of time is set as  $\tau = \sigma\sqrt{m/\epsilon}$ .

First, we prepare the polycrystalline sample as shown in Fig. 1. A polycrystalline structure is made as follows: The binary mixture is heated at the temperature of  $2.0\epsilon/k_B$  for  $50\tau$ , and then the temperature is reduced to  $0.001\epsilon/k_B$  rapidly over a span of  $5\tau$  and then equilibrated for another  $5\tau$  at the same temperature. The equations of motion are solved numerically using the time-reversible measure-preserving Verlet and reversible reference system propagator algorithms integration scheme with a time step  $\Delta t = 0.005\tau$ . The temperature of the system is controlled by connecting to a Nosé-Hoover thermostat. Finally, the remanent kinetic energy is drained out by performing  $NVE$  simulations with a viscous drag of  $1.0\epsilon\tau/\sigma^2$  over a time span of  $250\tau$ , as done in Ref. [30].

The dynamics under the deformation is athermal quasistatic [31,32]. Lees-Edwards periodic boundary conditions are employed. In each deformation step, a small strain increment of  $10^{-3}$  is followed by energy minimization using the conjugate gradient method. The strain is applied in a periodic manner: First, positive strain steps are applied. When a maximal predecided strain  $\gamma_0$  is reached, the strain is reversed by applying strain steps in the opposite direction. This proceeds until the strain reaches the negative value of the maximal strain  $-\gamma_0$ . At this point, the strain steps are reversed until the system returns to zero strain, completing the cycle ( $0 \rightarrow \gamma_0 \rightarrow 0 \rightarrow -\gamma_0 \rightarrow 0$ ). The cycle is then repeated  $n_{\text{max}} = 200$  times. The position of all atoms was saved at the end of every cycle. We applied the deformation to 5 to 10 samples prepared independently.

The deformation of the sample is carried out in two different ways. In one case, we apply volume-preserving periodic shear strain (SS) along the  $xy$  plane by incrementing the strain via the coordinate transformation of  $x' = x + yd\gamma_{xy}$  and  $y' = y$ . In the other case, we apply the deformation along the  $x$  direction. Specifically, when there is an elongation of the sample along the  $x$  directions, to preserve the volume, there is compression along the  $y$  direction, and during the  $x$ -axis

compression, elongation along the  $y$  direction is conducted, which is called periodic tensile-compressive strain (TCS). Volume-preserving cyclic deformation is a well-accepted approach employed to explore the yielding, irreversibility transition, etc., of colloidal suspensions, amorphous solids, and polycrystals [11,18,27,32,33]. In a passing note, in systems with high particle density, the dynamics are primarily influenced by particle-particle interactions rather than particle-solvent interactions [34]. Therefore, the solvent effect is negligible. When dealing with attractive colloidal particles, one common approach is to employ the square well potential [35], the Lennard-Jones (LJ) potential shifted by the diameter of the particle [36,37]. The simulations are performed using LAMMPS [38].

### III. RESULTS AND DISCUSSION

In 2D triangular colloidal crystals, five- and seven-coordinated particles, known as positive (+1) and negatively charged disclinations (−1), exist as defects. The likelihood of an individual disclination occurring is low. However, combining five- and seven-coordinated particles with small additional energy creates edge dislocations. A regular array of dislocations then forms a grain boundary separating differently oriented crystals, as shown in Fig. 1. Careful study shows that arrays of dislocations are mainly arranged along the grain boundaries and create a large difference in the orientation of the adjacent grains, which is consistent with Frank condition,  $\rho \propto \sin d\xi$ , where  $\rho$  is the line density (arrays of dislocations) along the grain boundary and  $d\xi$  represents the difference in orientation of the adjacent grains separated by the grain boundaries. In Fig. 1, we display the grain orientation of a sample before and after the completion of 200 cycles with a range of values of strain amplitudes for both modes of deformation. The properties of polycrystalline samples are primarily influenced by the number of dislocations and impurities along the grain boundaries. We maintain a fixed density of the larger particles, which serve as impurities, and examine the disclination density across 10 samples. The resulting average is  $0.061\sigma^{-2} \pm 0.001\sigma^{-2}$ , which suggests a small sample-to-sample variation. The top row corresponds to the tensile-compressive strain except for the panel on the far left, which displays a sample without any deformation, and the bottom row shows shear strain. When the amplitudes of the deformation are  $\gamma_0^{\text{TCS}} = 0.01, 0.021$  and  $\gamma_0^{\text{SS}} = 0.02, 0.03, 0.04$ , after a limit cycle, the sample responses reverse. However, when  $\gamma_0^{\text{TCS}} = 0.03$  and  $\gamma_0^{\text{SS}} = 0.055$ , a single crystal is seen in both modes of deformation.

*Enhanced mobility.* Depending on the strain amplitude, the local rearrangements of particles can be reversible after one or more cycles or irreversible, leading to chaotic dynamics and particle diffusion [33]. To characterize particle motion under cyclic deformation, we compute mean square displacement (MSD)  $\langle \Delta r^2 \rangle$  at the end of each cycle  $n$ , considering the initial configuration ( $n = 0$ ) as a reference, which is defined as follows:

$$\langle \Delta r^2(n) \rangle = \frac{1}{N} \left\langle \sum_{i=1}^N |\mathbf{r}_i(n) - \mathbf{r}_i(0)|^2 \right\rangle. \quad (2)$$

We plot the MSD as a function of the number of cycles for TCS and SS in Figs. 2(a) and 2(b), respectively. The results reveal that for a small strain amplitude, after a couple of cycles, particles exhibit a reversible behavior. However, with the increase in the strain amplitudes, it takes more and more cycles to eventually exhibit the reversible behavior. When  $\gamma_0^{\text{TCS(SS)}}$  is larger than the threshold value, we see that the system does not display any more reversibility within the explored time window, corresponding to irreversible, nonperiodic particle trajectories, and  $\langle \Delta r^2 \rangle$  there scales as  $\langle \Delta r^2 \rangle \sim n$ . To quantify the mobility, we measure the local slope  $d\langle \Delta r^2 \rangle / dn$  of the  $\langle \Delta r^2 \rangle$  vs  $n$  plot and average over the steady states and denote the average as diffusivity  $\mathcal{D}$ , as we did in our previous work [18,27]; a similar approach was used in Refs. [9,39,40]. In Fig. 2(c), we depict  $\mathcal{D}$  as a function of strain amplitudes  $\gamma_0^{\text{TCS(SS)}}$ . The results show that for a low strain amplitude, the particle diffusivity vanishes at steady state; that is, as expected,  $\mathcal{D} \approx 0$ . However, after a threshold value that appears as  $\gamma_{0,t}^{\text{TCS}} = 0.026$  and  $\gamma_{0,t}^{\text{SS}} = 0.0475$ , the system exhibits a significant jump in  $\mathcal{D}$  and becomes diffusive within the simulation timescale. The responses are similar in both modes of deformation. However, threshold strain amplitude in the SS mode is larger by approximately a factor of 2 compared to the TCS mode. In tensile-compressive loading, the amplitude of the applied strain is associated with deformation along the  $x$  direction. However, to maintain the volume of the simulation box, elongation in the  $x$  direction necessitates a simultaneous compression along the  $y$  direction. As a result, the material effectively undergoes deformation in both the  $x$  and  $y$  directions, a factor of 2 greater than the strain applied along the  $x$  direction. In contrast, when dealing with volume-preserving shear deformation, no such phenomenon occurs. The geometric distinctions between these two deformation modes are linked to a twofold shift. In our previous work, we found a threshold value of 0.044 for oscillatory shear deformation at temperature  $T = 0.001$  [18,27]. Most likely, the difference appeared because of the different deformation protocols. Several experiments and simulations have attempted to quantify the nature of the reversible to irreversible transition. Experiments with colloidal suspensions and numerical models show that the transition from reversible to irreversible is a second-order nonequilibrium phase transition [4]. However, a numerical study with jammed solids shows the transition as nonequilibrium first order [40]. However, an alternative explanation was also proposed [31,41] which relies on the chaotic nature of trajectories in dynamical systems but not the phase transition as a requirement to explain the relatively sharp onset of irreversibility observed in the experiments. In the present system, we recognize that near irreversible transitions,  $\mathcal{D}$  decreases by 1–2 orders of magnitude, which can be scaled algebraically,  $\mathcal{D} \sim (\gamma_0^{\text{TCS(SS)}} - \gamma_{0,t}^{\text{TCS(SS)}})^\alpha$ , with  $\alpha = 0.64$  and 1.54 for TCS and SS, respectively, as  $\gamma_{0,t}^{\text{TCS(SS)}}$  is approached from above [see Fig. 2(d)]. A recent study in which two-dimensional, amorphous solids under oscillatory shear were investigated showed the diffusion coefficient above the transition follows power-law scaling with an exponent of  $1.217 > 1$  [42], while in the case of a three-dimensional LJ glass, the exponent appeared to be 0.61 for low temperature and 0.54 for high temperature [39].

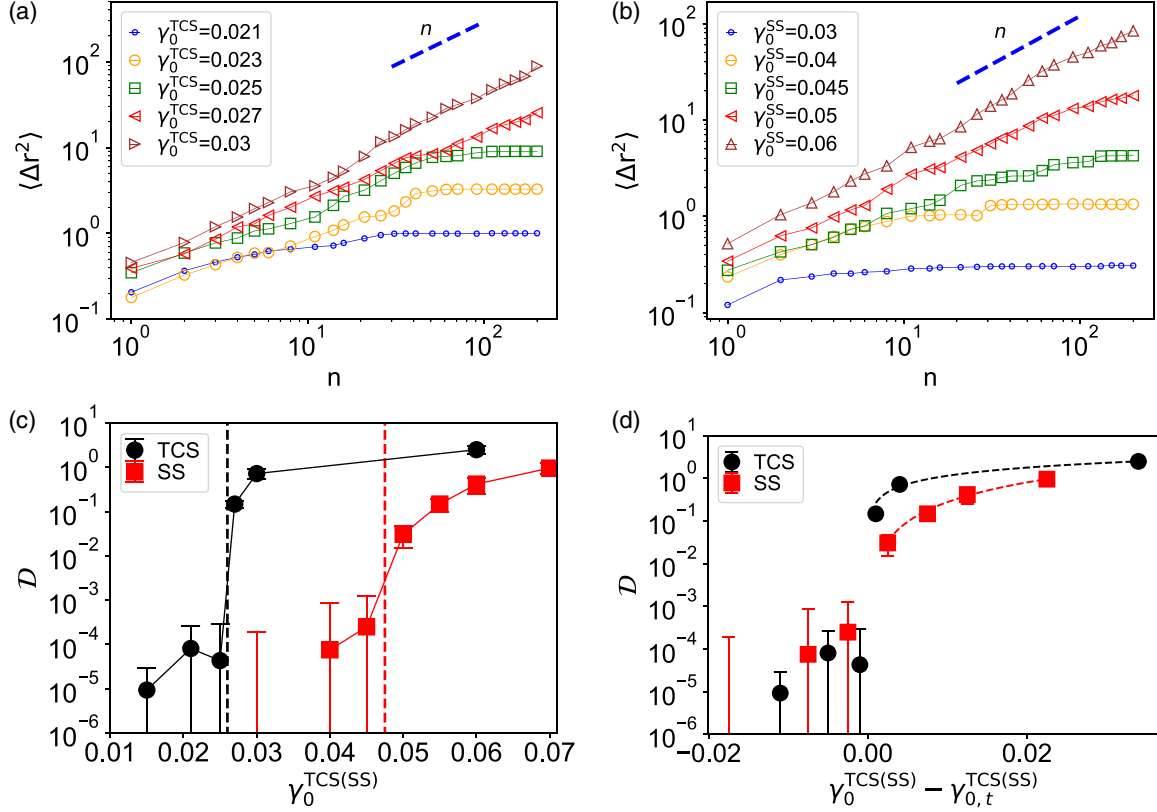


FIG. 2. MSD as a function of the number of cycles  $n$  for (a) TCS and (b) shear strain. (c) The local slope averaged over within the last 50 cycles  $D$  is shown as a function of strain amplitudes for TCS and shear strain. The dashed lines indicate the threshold strain amplitudes  $\gamma_{0,t}^{\text{TCS(SS)}}$ . (d)  $D$  is shown as a function of  $\gamma_0^{\text{TCS(SS)}} - \gamma_{0,t}^{\text{TCS(SS)}}$ . The dashed lines indicate  $D \sim [\gamma_0^{\text{TCS(SS)}} - \gamma_{0,t}^{\text{TCS(SS)}}]^\alpha$ , with  $\alpha = 0.64$  and  $1.54$  for TCS and SS, respectively.

**Hexatic order parameter.** To further quantify how the merging of grains influences the local structure, we measure the 2D local bond-orientational order parameter  $\psi_6$  for each particle  $i$  and plot the results in Fig. 3. The 2D local bond-orientational order parameter  $\psi_6$  for each particle  $i$  is defined as

$$\psi_6(r_{ij}) = \frac{1}{q} \sum_{j=1}^q e^{i6\theta(r_{ij})}, \quad (3)$$

where the summation is over all  $q$  nearest neighbors of the particle  $i$ .  $\theta$  is the angle between the vector  $\mathbf{r}_{ij}$  connecting particle  $i$  to  $j$  and the  $x$  axis. In the case of perfect hexagonal symmetry,  $|\psi_6| = 1$ , and  $\langle |\psi_6| \rangle > 0.7$  indicates that the system is crystalline [43,44]. In our systems, the particles with five or seven neighbors (dislocations) exhibit  $\langle |\psi_6| \rangle \approx 0.525$ , and for an initial configuration, their density is  $\approx 5.8\%$  (the remaining  $\approx 94\%$  of particles have hexatic symmetry and display  $\langle |\psi_6| \rangle \approx 0.985$ ). Therefore, our study samples display  $\langle |\psi_6| \rangle \gtrsim 0.95$ . Under deformation,  $\langle |\psi_6| \rangle$  even possess the larger value (until  $\gamma_0^{\text{TCS}} = 0.027$  and  $\gamma_0^{\text{SS}} = 0.055$ ), as shown in Figs. 3(a) and 3(b). The fraction of particles with the largest  $|\psi_6|$  also increases, as shown in Figs. 3(c) and 3(d). This indicates that the dislocations, i.e., particles with five or seven neighbors, disappear and exhibit perfect hexatic symmetry. The disappearance of dislocations occurs continuously with

large fluctuations close to the threshold  $\gamma_{0,t}^{\text{TCS(SS)}}$ , indicated by the dashed blue lines in Figs. 3(a) and 3(b). Similar behavior is observed in the distribution of hexatic order parameters. A further increase in strain amplitude reduces the order parameters, the fraction of particles with the largest  $|\psi_6|$  decreases, and the maximum appears at a slightly lower  $|\psi_6|$  for  $\gamma_0^{\text{TCS}} = 0.06$  and  $\gamma_0^{\text{SS}} = 0.12$ . A similar behavior was observed when shear-induced melting and crystallization were investigated by confocal microscopy in concentrated colloidal suspensions of hard-sphere-like particles [43]. A possible reason is that the particles move along a zigzag path [45–48] and they experience more collisions than without shear. Together with the hydrodynamics under shear, this leads to a larger mean square displacement and thus larger deviations from hexagonal symmetry [48]. In the inset of Fig. 3(b), we display  $\langle |\psi_6| \rangle$  vs  $\gamma_0^{\text{TCS(SS)}} - \gamma_{0,t}^{\text{TCS(SS)}}$  for both modes of deformation. The results show that one can access larger ordering in shear deformation than the tensile-compressive strain. This is connected to the larger diffusivity in the TCS mode after the threshold value than in the SS mode. To be precise, when we increase the strain amplitude, the number of cycles before reversibility is achieved rises. Consequently, there is a greater degree of particle mobility, leading to the annihilation of defects and an increase in the hexatic order parameters. In a passing note,

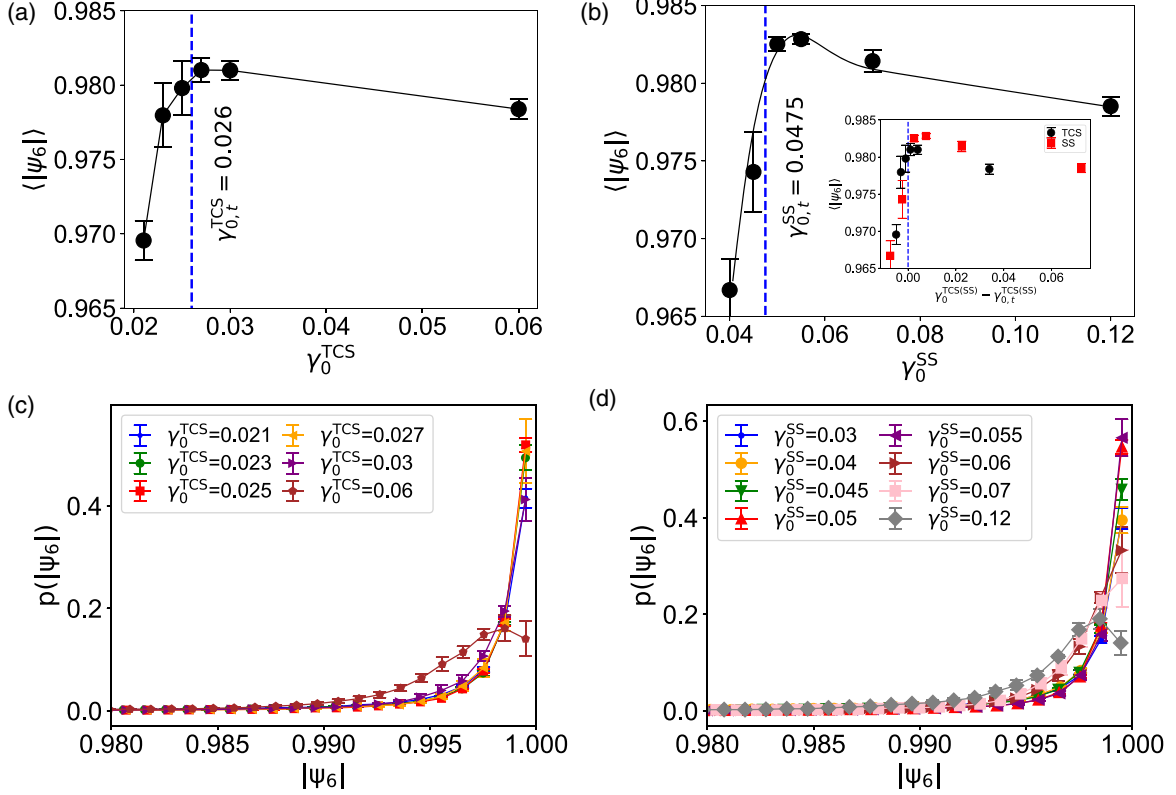


FIG. 3. Average hexatic order parameter  $\langle |\psi_6| \rangle$  as a function of (a) tensile-compressive strain amplitude  $\gamma_0^{\text{TCS}}$  and (b) shear strain amplitude  $\gamma_0^{\text{SS}}$ . The dashed blue line indicates the threshold value of the irreversible transition. In the inset we display  $\langle |\psi_6| \rangle$  as a function of  $\gamma_0^{\text{TCS(SS)}} - \gamma_{0,t}^{\text{TCS(SS)}}$ . Distribution of the hexatic order parameter  $|\psi_6|$  under (c) tensile-compressive and (d) shear strain for different values of amplitudes. The solid lines are a guide to the eye.

in soft systems like colloidal glasses, this connection between the irreversibility transition and structural change is complex and debated. Recent research showed that the yielding transition of colloidal glass in oscillatory shear can be detected through the static structure of the system [49]. However, computer simulations differ from that conclusion and argue that yielding is revealed through the dynamic evolution of the system [40].

**Atomic strain.** To understand the plastic deformation at the particle level in both modes of deformation, we look at the von Mises shear stress  $\eta$  [50]. The following algorithm is used: The initial configuration is considered as a reference, and the local transformation matrix  $\mathbf{J}_i$  that best maps  $\{\mathbf{d}_{ji}^0\} \rightarrow \{\mathbf{d}_{ji}\} \forall j \in P_i^0$  is formed, where  $\mathbf{d}$  are vector separations (row vectors) between atom  $j$  and  $i$  (a superscript 0 indicates the reference configuration). Here,  $j$  is one of atom  $i$ 's nearest neighbors, and  $P_i^0$  is the total number of nearest neighbors of atom  $i$  at the reference configuration.  $\mathbf{J}_i$  is determined by minimizing  $\sum_{j \in P_i^0} |\mathbf{d}_{ji}^0 \mathbf{J}_i - \mathbf{d}_{ji}|^2 \rightarrow \mathbf{J}_i$ . For each  $\mathbf{J}_i$ , the local Lagrangian strain matrix is computed as  $\eta_i = \frac{1}{2}(\mathbf{J}_i \mathbf{J}_i^T - \mathbf{I})$ . Then, the local shear invariant is calculated for each atom as

$$\eta_i = \sqrt{\eta_{xy}^2 + \frac{(\eta_{xx} - \eta_{yy})^2}{2}}, \quad (4)$$

and the atomic hydrostatic volumetric strain can be read as

$$\delta_i = \frac{\Delta V}{V} \approx \frac{\eta_{xx} + \eta_{yy}}{2}. \quad (5)$$

We measure the local shear invariant of individual particles after the completion of each cycle  $n$  with respect to the initial configuration, i.e.,  $n_{\text{ref}} = 0$ , and the average  $\langle \eta_{n_{\text{ref}}=0}^n \rangle$  is plotted as a function of  $n$  in Figs. 4(a) and 4(b) for tensile-compressive and shear strain, respectively. Qualitatively similar behaviors are observed, as in the case of particle mobility (see Fig. 2). When  $d\langle \eta_{n_{\text{ref}}=0}^n \rangle / dn$  is measured as a function of  $n$  for different values of  $\gamma_0^{\text{TCS(SS)}}$ , the observed large transient fluctuations in  $d\langle \eta_{n_{\text{ref}}=0}^n \rangle / dn$  close to the transition indicates the crackling noise, which is a signature of the nonequilibrium transition of grain boundary depinning (data not shown). This echoes the analogous behavior observed in  $d\langle \Delta r^2 \rangle / dn$  versus  $n$  for different  $\gamma_0^{\text{TCS(SS)}}$  (data not shown). Given these findings, we are inclined to adopt a methodology similar to that for diffusivity—a widely accepted metric for measuring the transition from reversible to irreversible processes. We measured local slope  $d\langle \eta_{n_{\text{ref}}=0}^n \rangle / dn$  from the  $\langle \eta_{n_{\text{ref}}=0}^n \rangle$  vs  $n$  plot and averaged over the steady states, denoted as  $\mathcal{F}$ , and the result is shown as a function of strain amplitudes  $\gamma_0^{\text{TCS(SS)}}$  in Fig. 4(c) for TCS and SS. The threshold strain amplitude appears the same as we see in the case of particle mobility. Further analysis reveals that the rate of change of the strain

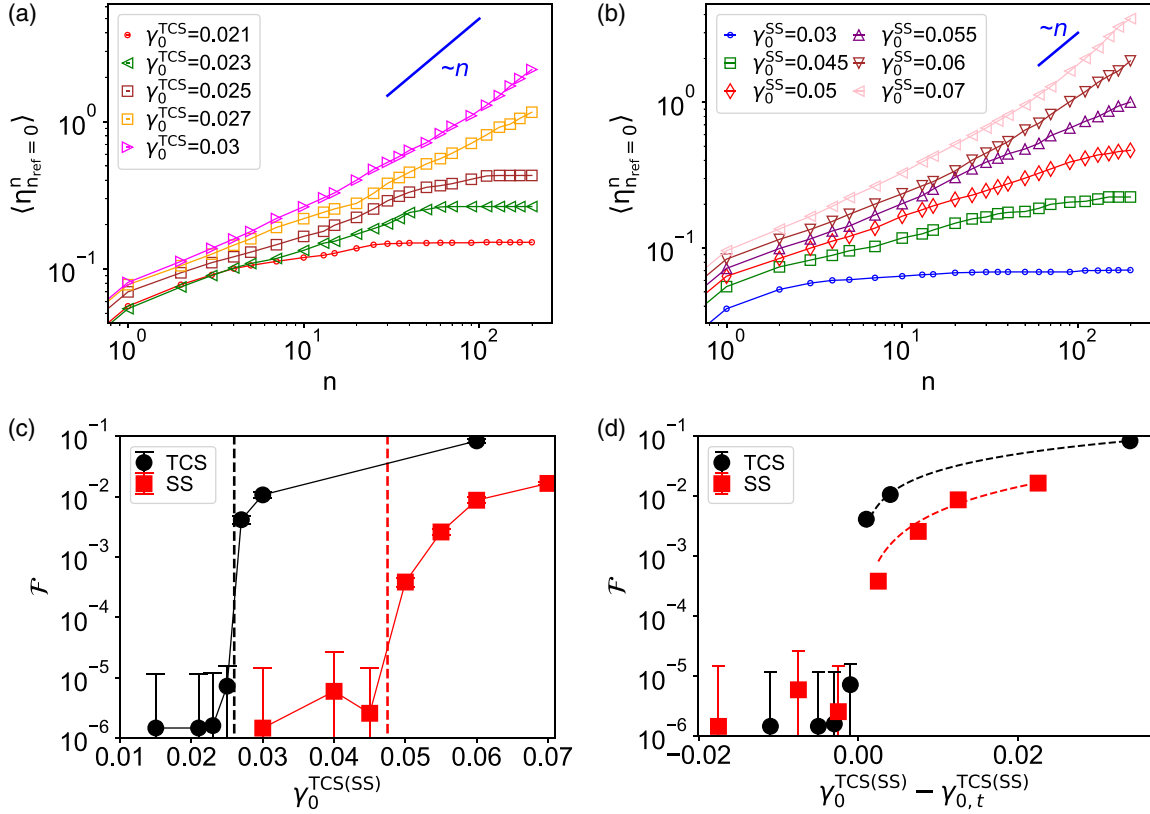


FIG. 4. Average of von Mises shear strain ( $\langle \eta_{n_{\text{ref}}=0}^n \rangle$ ) as a function of the number of cycles  $n$  for (a) TCS and (b) shear strain. (c) Local slope averaged over within the last 50 cycles  $\mathcal{F}$  is shown as a function of strain amplitudes for TCS and shear strain. The dashed lines indicate the threshold strain amplitudes  $\gamma_{0,t}^{\text{TCS(SS)}}$ . (d)  $\mathcal{F}$  is shown as a function of  $\gamma_0^{\text{TCS(SS)}} - \gamma_{0,t}^{\text{TCS(SS)}}$ . The dashed lines indicate  $\mathcal{F} \sim [\gamma_0^{\text{TCS(SS)}} - \gamma_{0,t}^{\text{TCS(SS)}}]^\beta$ , with  $\beta = 0.94$  and  $1.38$  for TCS and SS, respectively.

accumulation above the threshold amplitude is larger in the case of TCS than in the case of SS. The increment scales as  $\mathcal{F} \sim (\gamma_0^{\text{TCS(SS)}} - \gamma_{0,t}^{\text{TCS(SS)}})^\beta$ , with  $\beta = 0.94$  and  $1.38$  for TCS and SS, respectively [see Fig. 4(d)].

To further understand the atomic strain of individual particles, we measure the distribution of  $\eta$  after completion of  $n_{\text{max}} (= 200)$  cycles with respect to the initial configuration  $P(\eta_{n_{\text{ref}}=0}^{n_{\text{max}}})$  and display the results in Figs. 5(a) and 5(c) for tensile-compressive and shear strain, respectively. Under tensile-compressive deformation, when the strain amplitude is kept at a low value, such as  $\gamma_0^{\text{TCS}} = 0.021$ , approximately 39% of the particles are found within a region where  $\eta_{n_{\text{ref}}=0}^{n_{\text{max}}} < 0.04$ , and they are situated in the interior of the grains. Notably, distinct peaks emerge at  $\eta_{n_{\text{ref}}=0}^{n_{\text{max}}} \approx 0.1$  and at  $0.3$ , which can be attributed to dislocation motions occurring through the grains [see Fig. 6(a)]. Furthermore, particles experiencing even higher strain are observed because of the dislocation motions near the grain boundaries. Moreover, as the value of  $\gamma_0^{\text{TCS}}$  increases, as anticipated, the occurrence of particles with a strain below  $0.04$  becomes less frequent [see Figs. 6(b) and 6(c)]. Nevertheless, the distinct peaks at approximately  $0.1$  and  $0.3$  in the  $\eta_{n_{\text{ref}}=0}^{n_{\text{max}}}$  distribution persist even with the increase in  $\gamma_0^{\text{TCS}}$ . Similar dynamics are evident under shear deformation when  $0.03 \leq \gamma_0^{\text{SS}} \approx \gamma_{0,t}^{\text{SS}}$ , as clarified in the strain map in Figs. 6(d) and 6(e). However, for  $\gamma_0^{\text{SS}} = 0.01$  and  $0.02$ , no additional peaks are present. Instead, we observe a

power-law distribution with an exponent of  $-1.54$ . In this range of strain amplitudes, strain accumulation occurs primarily due to the motion of defects near the grain boundaries rather than the motion of the defect through the grains. To be precise, depending on the strain amplitude, we have observed two distinct mechanisms of plastic deformation in polycrystalline systems: dislocations may move through the grains, eventually forming slip lines in two dimensions. Second, particles at the grain boundaries undergo local rearrangements, leading to grain boundary motions. These two types of motion were previously reported in the study by Shiba and Onuki [51]. In a passing note, in the case of colloidal glass, the second type of rearrangement (referring to the motion of particles at the grain boundaries) is predominantly observed [52,53].

In Figs. 5(b) and 5(d), we show the distribution of  $p(\eta_{n_{\text{ref}}=0}^{n_{\text{max}}}/\langle \eta_{n_{\text{ref}}=0}^{n_{\text{max}}} \rangle)$  for TCS and SS, respectively, and data collapse reasonably with expected differences before and after the threshold strain amplitudes. For both modes of deformation, when  $\gamma_0^{\text{TCS(SS)}} > \gamma_{0,t}^{\text{TCS(SS)}}$ , the motion of the dislocations through crystals dominates the distribution. However, a key difference is that the strain is accumulated diagonally in tensile-compressive loading [see Fig. 6(c)], whereas in the case of shear loading, the strain accumulation is either along the  $x$  axis or along the  $y$  axis, as shown in Figs. 6(e) and 6(f). This observation can be understood based on the Peach-Koehler theory, from which one can write the elastic energy

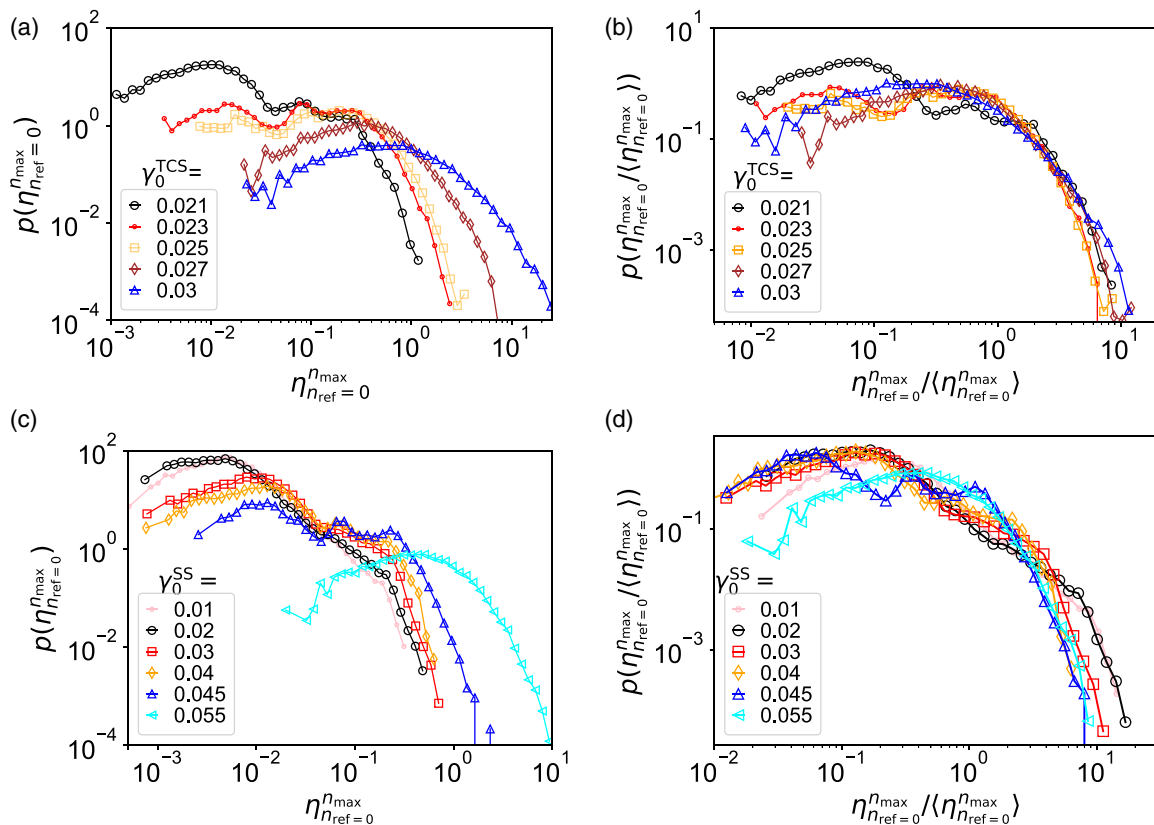


FIG. 5. Distribution of von Mises shear strain measured after completion of  $n_{\max}(= 200)$  cycles for the (a) TCS and (c) shear strain with respect to the initial configuration. The data are collapsed using average accumulated strain and are shown in (b) and (d) for TCS and shear strain, respectively.

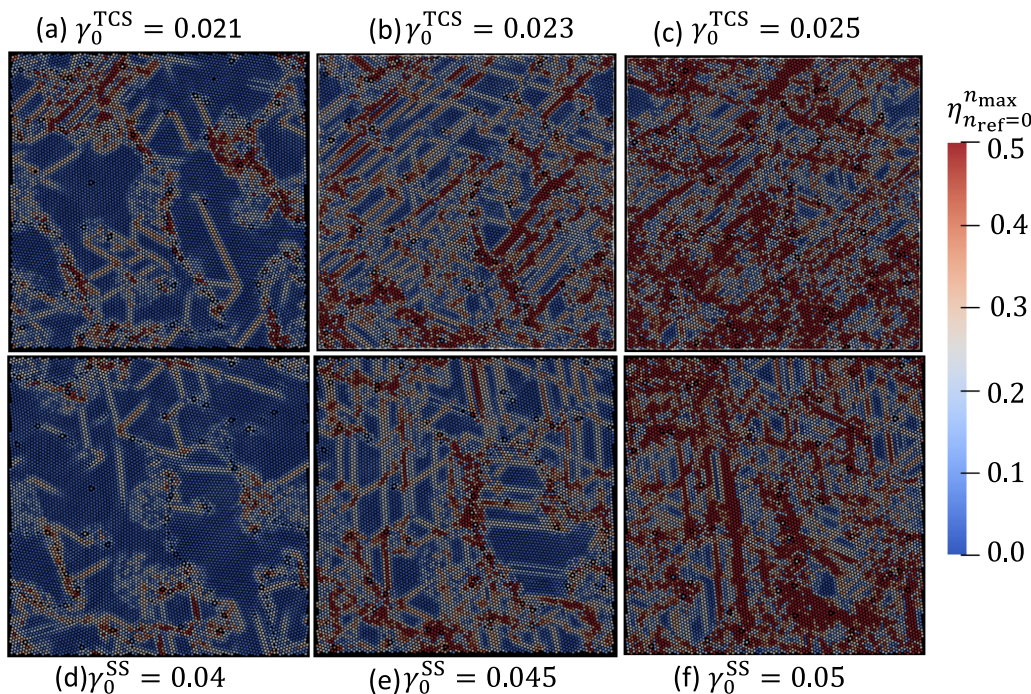


FIG. 6. von Mises shear strain map for individual particles after 200 cycles. It is measured with respect to the initial configurations. The top row corresponds to TCS, and the bottom row shows shear strain. The strain amplitude is specified. For the TCS, the strain accumulates diagonally, and for the shear loading, strain is accumulated along the  $x$  or  $y$  axis.

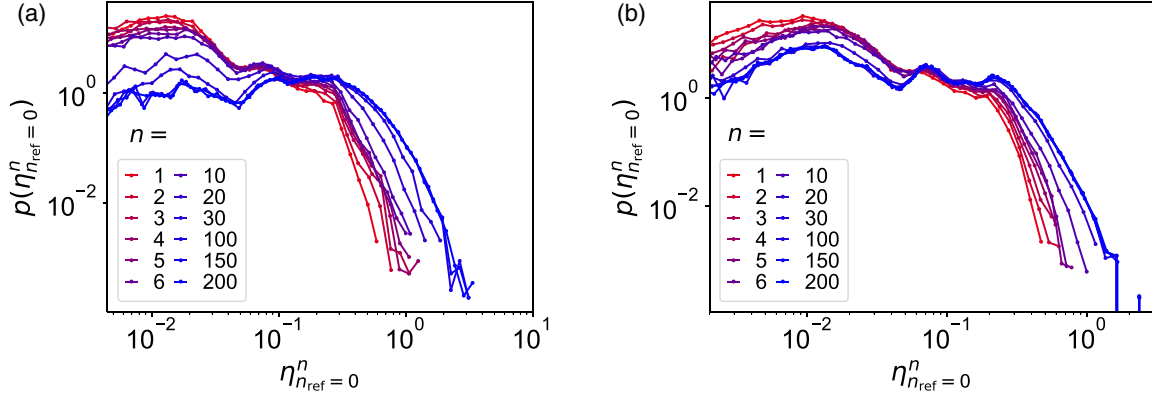


FIG. 7. von Mises shear strain of an individual particle is measured after  $n$  cycles with respect to the initial configuration, i.e.,  $n_{\text{ref}} = 0$ , and the distribution is displayed. (a) is for  $\gamma_0^{\text{TCS}} = 0.025$ , and (b) is for  $\gamma_0^{\text{SS}} = 0.045$ .

of the slip in isotropic elasticity as

$$F_{\text{slip}} = \frac{Gb^2}{2\pi} \frac{\ln(\mathcal{L}/b)}{1-\nu} \pm \sigma_{xy}^{\text{ext}} b\mathcal{L} \cos(2\phi). \quad (6)$$

The first term is the elastic energy of the dislocations, and the second is the work of the applied force. The  $\pm$  sign indicates the direction of motion of the particles around the slip line,  $b$  is the lattice constant,  $\mathcal{L}$  is the slip length,  $G$  is the shear modulus,  $\nu$  is Poisson's ratio, and  $\phi$  is the angle between the slip direction and the  $x$  axis. For shear deformation with  $\sigma_{xy}^{\text{ext}} > 0$ , when we use  $+$ , we can achieve the lowest  $F_{\text{slip}}$  for  $\phi = 0$  (i.e., the slip is along the  $x$  axis), and when we use  $-$ , the slip is along the  $y$  axis as  $\phi = \pi/2$ . For uniaxial deformation  $\sigma_{\alpha}^{\text{ext}}$ , we can write an analogous equation as follows:

$$F_{\text{slip}} = \frac{Gb^2}{2\pi} \frac{\ln(\mathcal{L}/b)}{1-\nu} \pm \sigma_{\alpha}^{\text{ext}} b\mathcal{L} \sin(2\phi), \quad (7)$$

and the preferred orientation of the slip line is  $\pm\pi/4$ . These preferred directions have been observed in amorphous metals [28,54] and granular materials [29,55]. In simulations, shear bands in these preferred directions were realized in model amorphous metals and polymers [56–61] and in a model crystal with weak elastic anisotropy [62].

To further analyze the atomic strain, we compute  $p(n_{n_{\text{ref}}=0}^n)$  after each  $n$  for  $\gamma_0^{\text{TCS}} = 0.025$  [see Fig. 7(a)] and  $\gamma_0^{\text{SS}} = 0.045$  [see Fig. 7(b)], which are close to  $\gamma_{0,t}^{\text{TCS(SS)}}$  and in the reversible regime. Under the TCS ( $\gamma_0^{\text{TCS}} = 0.025$ ) deformation, we observe that rearrangements around the grain boundaries and dislocation motions through the grains are activated immediately after the first cycle. However, it is worth noting that more than 50% of the particles (approximately 58%) remain in the strain regime where the strain  $\langle n_{n_{\text{ref}}=0}^n \rangle$  is less than 0.04. As the number of cycles  $n$  increases, the situation evolves. At  $n = 30$ , we observe indications of two additional peaks in the probability distribution function  $p(n_{n_{\text{ref}}=0}^n)$ . However, these peaks become smeared out when  $n = 200$ . On the other hand, in the case of shear strain ( $\gamma_0^{\text{SS}} = 0.045$ ), the two additional peaks remain clearly visible in the strain regime under investigation even at  $n = 200$ . However, a situation similar to that for tensile-compressive deformation (i.e., peaks become smeared out when  $n = 200$ ) emerges for  $\gamma_0^{\text{SS}} = 0.05$ . We observe a resemblance in the behavior of atomic rearrangements be-

tween the two cases, indicating the common characteristics in the strain response under both shear and tensile-compressive deformations.

To identify and characterize the two additional peaks in both modes of deformation, we compute the von Mises shear strain for individual particles at cycle number  $n$  with respect to the previous cycle,  $n - 1$ , instead of taking the configuration where  $n = 0$  as a reference. The distribution and the strain map are shown in Figs. 8 and 9, respectively, for  $\gamma_0^{\text{TCS}} = 0.03$  and  $\gamma_0^{\text{SS}} = 0.055$ , which are in the irreversible regime where the defect motion through crystal dominates. Two clear peaks are observed in both cases [see Figs. 8, 9(a), and 9(b)]. When dislocations move through the crystals, the particles at the adjacent grains exhibit either clockwise or counterclockwise rotation. See the displacement field in Fig. 9(c). This type of rotation leads to the merging of grains with different orientations and creates a single-grain structure.

Last, we evaluate the volumetric strain  $\delta$  of each particle using Eq. (5), and their distributions are displayed in Figs. 10(a) and 10(b) for different values of TCS and SS amplitudes, respectively. When the shear strain ampli-

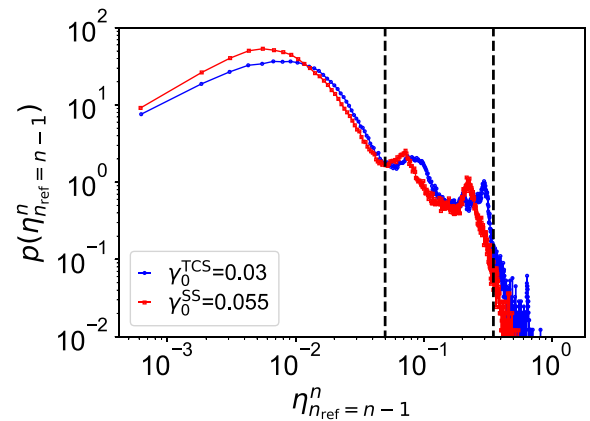


FIG. 8. von Mises shear strain of an individual particle is measured after each cycle  $n$  with respect to the configuration after  $n - 1$  cycles, and the distribution averaged over the first 20 cycles is displayed. For both tensile-compressive and shear strains, two peaks appear between 0.05 and 0.35.



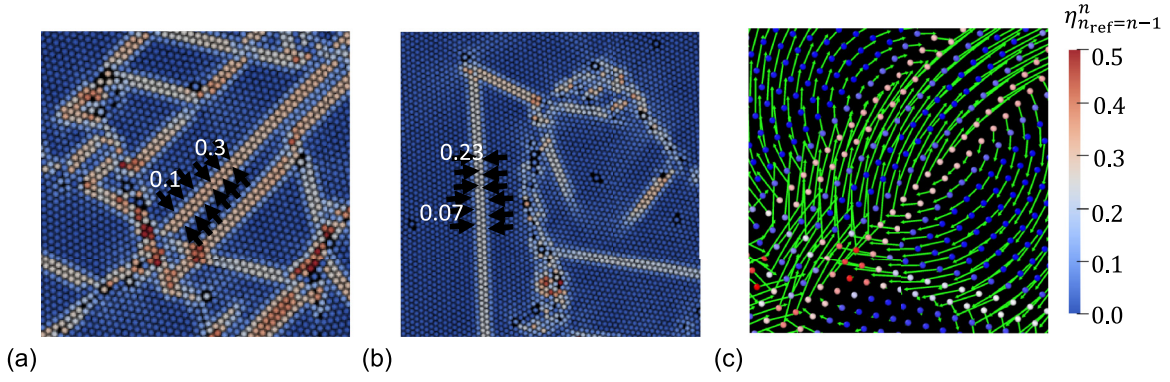


FIG. 9. von Mises shear strain map for individual particles measured with respect to the previous configuration to display the dislocation motions through crystals. (a) is for  $\gamma_0^{\text{TCS}} = 0.03$ , and (b) is for  $\gamma_0^{\text{SS}} = 0.055$ . (c) Displacement map corresponding to the motion of the defect in oscillatory TCS. The arrow indicates the direction of the displacement.

tude is small [see  $\gamma_0^{\text{SS}} = 0.02$  in Fig. 10(b)], we observe a symmetrical distribution centered around  $\delta = 0$ . However, with the increase of  $\gamma_0^{\text{SS}}$  (say, 0.04 or 0.045), the distribution becomes positively skewed, and the additional peak appears and grows at around  $0.05 \pm 0.01$  [see the inset of Fig. 10(b)]; the peak height decreases when the strain amplitude approaches the threshold value. This additional peak in volumetric strain is also a signature of dislocation motion through the grains. This motion through grains takes over

the volumetric strain distribution in the irreversible regime. Under tensile-compressive loading, the system behaves similarly [see Fig. 10(a) and its inset]. The evolution pattern of the additional peak over the cycles at a strain amplitude close to the threshold value appears nonmonotonic depending on the strain amplitude. We see the nonmonotonicity when  $\gamma_0^{\text{TCS}} = 0.025$ , as shown in Fig. 10(c), and  $\gamma_0^{\text{SS}} = 0.05$  (data not shown), while it is not at  $\gamma_0^{\text{SS}} = 0.045$  [see Fig. 10(d)]. In addition to that, we also observe a positive skewness in the

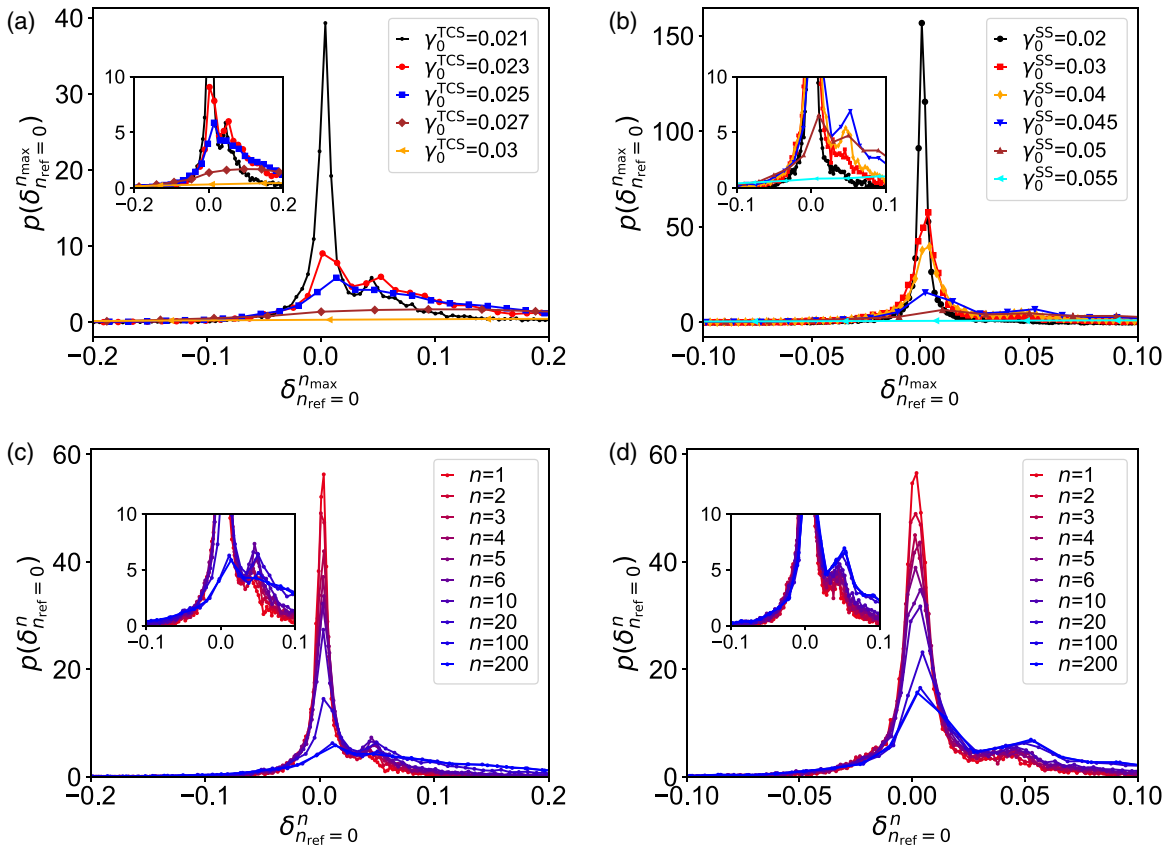


FIG. 10. (a) Distribution of volumetric strain of an individual particle  $\delta_i$  measured after  $n_{\text{max}} (= 200)$  cycles for different strain amplitudes of (a) tensile-compressive and (b) shear loading. The distribution is measured after each cycle  $n$  and is shown as indicated in the legends of (c) and (d). (c) is for tensile-compressive strain with  $\gamma_0^{\text{TCS}} = 0.025$ , and (d) is for shear strain with  $\gamma_0^{\text{SS}} = 0.045$ . The insets are zoomed in on the additional peak.

distribution as we apply more and more cycles. Additionally, we observe a significant correlation between the volumetric strain and the shear strain in both modes of deformation. This finding is consistent with previous observations in the case of metallic glasses [63], indicating a common behavior across different materials and deformation modes.

#### IV. CONCLUSIONS

The present study investigated the irreversible transition in a 2D polycrystalline sample under two distinct oscillatory deformation modes: Tensile-compressive and shear strain. Upon subjecting the material to both deformation modes, we observed a reversible elastic response up to a critical strain amplitude, beyond which irreversible plastic deformation occurs. Notably, the threshold strain amplitude required for the transition was found to be larger in the case of shear strain compared to the tensile-compressive deformation. To confirm the threshold values of the reversible-irreversible transition, we conducted dynamical analyses, including assessments of particle mobility and atomic strain. Additionally, we performed structural analyses, such as evaluating the hexatic order parameter. For particle mobility, we studied the MSD of the particles with respect to the initial configurations. From there, we defined diffusivity as the local slope of the MSD vs the number of cycles plot. We found that for both modes of deformation, the diffusivity decreases  $\approx 1$  to 2 orders of magnitudes close to the threshold value from the above, defined as the irreversible regime, and then jumps to  $\mathcal{D} \approx 0$  during the steady states, defined as the reversible regime. In a passing note, one may consider the average particle displacement after each cycle as a dynamic observable instead of the diffusivity from the MSD as done in Ref. [40]. This study also opens up the question of whether the nonequilibrium transition is continuous or discontinuous.

In the structural analysis, we observed that the hexatic order parameter increases as we increase the strain amplitude for both modes of deformation, which indicates the disappearance of grain boundaries and dislocations. A further increase in strain amplitudes lowers the order parameters.

To explore the strain at the particle level, we measured both von Mises shear strain and the volumetric strain. The change

in von Mises shear strain per cycle as a function of strain amplitude shows behavior qualitatively similar to that of diffusivity for both modes of deformation. We observed two types of dynamics: first, the local rearrangement of particles near the grain boundary leads to the grain boundary motion, and second, the motion of dislocation through the grains results in a slip line in two dimensions. Further analysis revealed that in the case of tensile-compressive shear, the strain accumulates (slip line) diagonally, whereas for shear strain, the strain accumulation occurs along the  $x$  and  $y$  directions. The nature of the strain accumulation was explained in terms of the Peach-Koehler theory. The volumetric strain analysis also captured the dislocation motion through the grains. Additionally, we observed a strong correlation between the von Mises shear strain and the volumetric strain.

Our findings reveal that colloidal polycrystals subjected to oscillatory shear and tensile-compressive strain exhibit an irreversibility transition similar to disordered particle assemblies and colloidal glasses. However, in this context, the relevant degrees of freedom are the topological defects rather than the particles themselves. The implications of our study extend to applications such as Zener pinning, where inclusions are strategically utilized to impede grain growth in polycrystals [64]. The critical strain amplitude for irreversibility that we identified should correspond to the depinning stress required to initiate grain boundary growth [65]. One could test our results in colloidal particle experiments [21–23]. This study could potentially expand into the realm of amorphous solids [32,33]. Our investigation revealed that the larger strain amplitude of irreversible transition in the SS mode is linked to deformation geometry. Based on this finding, we anticipate a similar effect in amorphous solids when they are subjected to these deformation modes.

#### ACKNOWLEDGMENTS

P.K.J. acknowledges the financial support from the Science and Engineering Research Board, Government of India (Grant No. SRG/2022/000993), and ACRG from BITS Pilani. Khushika acknowledges the financial support from the BITS Pilani, Pilani Campus Institute fellowship. The simulations were performed at the high-performance computing cluster of BITS Pilani, Pilani Campus.

- 
- [1] S. Slotterback, M. Mailman, K. Ronaszegi, M. van Hecke, M. Girvan, and W. Losert, *Phys. Rev. E* **85**, 021309 (2012).
  - [2] R. Möbius and C. Heussinger, *Soft Matter* **10**, 4806 (2014).
  - [3] J. R. Royer and P. M. Chaikin, *Proc. Natl. Acad. Sci. USA* **112**, 49 (2015).
  - [4] L. Corte, P. M. Chaikin, J. P. Gollub, and D. J. Pine, *Nat. Phys.* **4**, 420 (2008).
  - [5] E. Tjhung and L. Berthier, *Phys. Rev. Lett.* **114**, 148301 (2015).
  - [6] T. H. Besseling, M. Hermes, A. Fortini, M. Dijkstra, A. Imhof, and A. van Blaaderen, *Soft Matter* **8**, 6931 (2012).
  - [7] M. D. Haw, W. C. K. Poon, and P. N. Pusey, *Phys. Rev. E* **57**, 6859 (1998).
  - [8] P. A. Smith, G. Petekidis, S. U. Egelhaaf, and W. C. K. Poon, *Phys. Rev. E* **76**, 041402 (2007).
  - [9] D. Pine, J. P. Gollub, J. Brady, and A. Leshansky, *Nature (London)* **438**, 997 (2005).
  - [10] G. I. Menon and S. Ramaswamy, *Phys. Rev. E* **79**, 061108 (2009).
  - [11] P. Leishangthem, A. D. S. Parmar, and S. Sastry, *Nat. Commun.* **8**, 14653 (2017).
  - [12] N. V. Priezjev, *Comput. Mater. Sci.* **150**, 162 (2018).
  - [13] N. C. Keim and P. E. Arratia, *Soft Matter* **9**, 6222 (2013).

- [14] L. Pérez-Ocampo, A. Zaccone, and M. Laurati, *J. Rheol.* **62**, 197 (2018).
- [15] C. Reichhardt, I. Regev, K. Dahmen, S. Okuma, and C. J. O. Reichhardt, *Phys. Rev. Res.* **5**, 021001 (2023).
- [16] P. Das, H. Vinutha, and S. Sastry, *Proc. Natl. Acad. Sci. USA* **117**, 10203 (2020).
- [17] K. Nagasawa, K. Miyazaki, and T. Kawasaki, *Soft Matter* **15**, 7557 (2019).
- [18] P. K. Jana, M. J. Alava, and S. Zapperi, *Phys. Rev. E* **98**, 062607 (2018).
- [19] N. Hansen, *Scr. Mater.* **51**, 801 (2004).
- [20] D. M. Lobmeyer and S. L. Biswal, *Sci. Adv.* **8**, eabn5715 (2022).
- [21] N. Ghofraniha, E. Tamborini, J. Oberdisse, L. Cipelletti, and L. Ramos, *Soft Matter* **8**, 6214 (2012).
- [22] A. Louhichi, E. Tamborini, J. Oberdisse, L. Cipelletti, and L. Ramos, *Phys. Rev. E* **92**, 032307 (2015).
- [23] N. C. Keim and P. E. Arratia, *Soft Matter* **11**, 1539 (2015).
- [24] E. Tamborini, L. Cipelletti, and L. Ramos, *Phys. Rev. Lett.* **113**, 078301 (2014).
- [25] I. Buttinoni, M. Steinacher, H. T. Spanke, J. Pokki, S. Bahmann, B. Nelson, G. Foffi, and L. Isa, *Phys. Rev. E* **95**, 012610 (2017).
- [26] B. van der Meer, W. Qi, J. Sprakel, L. Filion, and M. Dijkstra, *Soft Matter* **11**, 9385 (2015).
- [27] P. K. Jana, M. J. Alava, and S. Zapperi, *Sci. Rep.* **7**, 45550 (2017).
- [28] C. A. Schuh, T. C. Hufnagel, and U. Ramamurty, *Acta Mater.* **55**, 4067 (2007).
- [29] J. Desrues, J. Lanier, and P. Stutz, *Eng. Fract. Mech.* **21**, 909 (1985).
- [30] C. Negri, A. L. Sellerio, S. Zapperi, and M. C. Miguel, *Proc. Natl. Acad. Sci. USA* **112**, 14545 (2015).
- [31] I. Regev, T. Lookman, and C. Reichhardt, *Phys. Rev. E* **88**, 062401 (2013).
- [32] A. D. S. Parmar, S. Kumar, and S. Sastry, *Phys. Rev. X* **9**, 021018 (2019).
- [33] I. Regev, J. Weber, C. Reichhardt, K. A. Dahmen, and T. Lookman, *Nat. Commun.* **6**, 8805 (2015).
- [34] F. van Swol and D. N. Petsev, *RSC Adv.* **4**, 21631 (2014).
- [35] E. Zaccarelli, G. Foffi, K. A. Dawson, S. V. Buldyrev, F. Sciortino, and P. Tartaglia, *Phys. Rev. E* **66**, 041402 (2002).
- [36] N. Patel and S. Egorov, *J. Chem. Phys.* **123**, 144916 (2005).
- [37] P. Santos, O. Campanella, and M. Carignano, *Soft Matter* **9**, 709 (2013).
- [38] S. Plimpton, *J. Comput. Phys.* **117**, 1 (1995).
- [39] D. Fiocco, G. Foffi, and S. Sastry, *Phys. Rev. E* **88**, 020301(R) (2013).
- [40] T. Kawasaki and L. Berthier, *Phys. Rev. E* **94**, 022615 (2016).
- [41] G. Düring, D. Bartolo, and J. Kurchan, *Phys. Rev. E* **79**, 030101(R) (2009).
- [42] I. Regev and T. Lookman, *J. Phys.: Condens. Matter* **31**, 045101 (2019).
- [43] Y. L. Wu, D. Derks, A. van Blaaderen, and A. Imhof, *Proc. Natl. Acad. Sci. USA* **106**, 10564 (2009).
- [44] K. H. Nagamanasa, S. Gokhale, R. Ganapathy, and A. Sood, *Proc. Natl. Acad. Sci. USA* **108**, 11323 (2011).
- [45] B. J. Ackerson, *J. Rheol.* **34**, 553 (1990).
- [46] M. J. Stevens and M. O. Robbins, *Phys. Rev. E* **48**, 3778 (1993).
- [47] M. J. Stevens, M. O. Robbins, and J. F. Belak, *Phys. Rev. Lett.* **66**, 3004 (1991).
- [48] D. Derks, Y. L. Wu, A. van Blaaderen, and A. Imhof, *Soft Matter* **5**, 1060 (2009).
- [49] D. V. Denisov, M. T. Dang, B. Struth, A. Zaccone, G. H. Wegdam, and P. Schall, *Sci. Rep.* **5**, 14359 (2015).
- [50] S. Futoshi, O. Shigenobu, and J. Li, *Mater. Trans.* **48**, 2923 (2007).
- [51] H. Shiba and A. Onuki, *Phys. Rev. E* **81**, 051501 (2010).
- [52] F. Spaepen, *Acta Metall.* **25**, 407 (1977).
- [53] M. L. Manning, J. S. Langer, and J. M. Carlson, *Phys. Rev. E* **76**, 056106 (2007).
- [54] Q. Wei, D. Jia, K. Ramesh, and E. Ma, *Appl. Phys. Lett.* **81**, 1240 (2002).
- [55] J. Desrues and R. Chambon, *Int. J. Solids Struct.* **39**, 3757 (2002).
- [56] D. Deng, A. Argon, and S. Yip, *Phil. Trans. R. Soc. Lond. A* **329**, 613 (1989).
- [57] Y. Shi and M. L. Falk, *Phys. Rev. B* **73**, 214201 (2006).
- [58] C. E. Maloney and M. O. Robbins, *J. Phys.: Condens. Matter* **20**, 244128 (2008).
- [59] N. P. Bailey, J. Schjøtz, and K. W. Jacobsen, *Phys. Rev. B* **73**, 064108 (2006).
- [60] V. Bulatov and A. Argon, *Modell. Simul. Mater. Sci. Eng.* **2**, 167 (1994).
- [61] A. Argon, V. Bulatov, P. Mott, and U. Suter, *J. Rheol.* **39**, 377 (1995).
- [62] A. Onuki, *Phys. Rev. E* **68**, 061502 (2003).
- [63] Y.-J. Wang, M. Jiang, Z. Tian, and L. Dai, *Scr. Mater.* **112**, 37 (2016).
- [64] P. Hazzledine and R. Oldershaw, *Philos. Mag. A* **61**, 579 (1990).
- [65] P. Moretti, M.-C. Miguel, M. Zaiser, and S. Zapperi, *Phys. Rev. B* **69**, 214103 (2004).